

Greenland supraglacial lake drainages triggered by hydrologically induced basal slip

Laura A. Stevens^{1*} †, Mark D. Behn², Jeffrey J. McGuire², Sarah B. Das², Ian Joughin³, Thomas Herring⁴, David E. Shean³, Matt A. King⁵

¹Massachusetts Institute of Technology/Woods Hole Oceanographic Institution Joint Program in Oceanography/Applied Ocean Science and Engineering, Woods Hole, MA 02543, USA

²Department of Marine Geology and Geophysics, Woods Hole Oceanographic Institution, Woods Hole, MA 02543, USA

³Polar Science Center, Applied Physics Lab, University of Washington, 1013 NE 40th St., Seattle, WA 98105-6698, USA

⁴Department of Earth, Atmospheric, and Planetary Sciences, Massachusetts Institute of Technology, Cambridge, MA 02139, USA

⁵School of Land and Food, University of Tasmania, Private Bag 76, Hobart, Tasmania, 7001, Australia

*stevensl@mit.edu

†360 Woods Hole Road, Woods Hole, MA 02543 USA

Abstract:

Water-driven fracture propagation beneath supraglacial lakes rapidly transports large volumes of surface melt-water to the base of the Greenland Ice Sheet¹. These drainage events drive transient ice-sheet acceleration^{1–3} and establish conduits for additional surface-to-bed melt-water transport for the remainder of the melt season^{1,4–6}. While it is well established that cracks must remain water-filled to propagate to the bed^{7–9}, the precise mechanisms that initiate hydro-fracture events beneath lakes are unknown. Here we show that, for a lake on the western Greenland Ice Sheet, drainage events are preceded by a 6–12 hour period of ice-sheet uplift and/or enhanced basal slip. Our observations from a dense GPS network allow us to determine the distribution of melt-water at the ice-sheet bed before, during, and after three rapid drainages in 2011–2013, each of which generates tensile stresses that promote hydro fracture beneath the lake. We hypothesize that these precursors are associated with the introduction of melt-water to the bed through

neighboring moulin systems (vertical conduits connecting the surface and base of the ice sheet). Our results imply that as lakes form in less crevassed, interior regions of the ice sheet^{10–14}, where water at the bed is currently less pervasive^{5,14–16}, the creation of new surface-to-bed conduits caused by lake-draining hydro-fractures may be limited.

Main Text:

Greenland ice sheet flow accelerates at the beginning of the melt-season^{5,15}, when surface melt-water reaches the bed via conduits^{1,4–6,17,18}. Inland from the ice margin, this process is often associated with the drainage of supraglacial lakes^{1,5,19}. The majority of supraglacial lakes drain slowly, overfilling their banks and routing lake water via surficial streams to nearby crevasses and/or moulins^{3,20,21}. A smaller fraction (~13%) of lakes drain rapidly (<1 day)²⁰, in some cases as rapidly as a few hours^{1–3}, through large (kilometer-scale length) hydro-fractures that form directly beneath the lake basin. These hydro-fractures subsequently close except where continued stream flow keeps moulins open for the remainder of the melt season^{1–3}. While the former style of drainage requires the presence of pre-existing crevasses and/or moulins, the latter style has the potential to create new surface-to-bed melt-water pathways through the ice sheet, and is thus an area of intense study^{1–3,5,19,22,23}.

While the basic principles of hydro-fracture through glacial ice are well understood^{7–9}, the mechanism that triggers the formation of kilometer-scale length hydro-fractures in compressional basins where lakes form is unknown². A necessary condition for generating through-ice hydro-fractures is that a supraglacial lake must contain a sufficient volume of water to keep a fracture filled as it propagates from the surface to the bed^{7–9}. However, large lakes

with volumes well above this threshold often do not drain over multiple summers¹². Additionally, lakes repeatedly fill basins containing numerous healed hydro-fracture cracks and moulins created during prior years' drainage events^{1,2,7}, implying that the presence of pre-existing cracks does not necessarily lead to immediate drainage. Thus, identifying the first-order control on hydro-fracture initiation preceding rapid lake drainages has remained elusive.

In this study, we investigate hydro-fracture initiation and rapid drainage at North Lake (68.72°N, -49.50°W), a ~2.5-km diameter supraglacial lake located south of the Jakobshavn-Isbrae catchment on thick ice (~980 m) (Fig. 1). This site has been the focus of in-depth study since 2006, when the first detailed evidence for hydro-fracture to the bed of the Greenland ice sheet was collected using Global Positioning System (GPS) measurements from North Lake base station¹ (NLBS) (Fig. 1). During the 2006 event, a slow, steady lake-level drop was observed over a 16-hour pre-drainage stage followed by the rapid (<2 hr) drainage coincident with vertical and horizontal ice displacement¹. Subsequent modeling of the NLBS data collected during this event found that vertical uplift was caused almost entirely by a horizontal cavity opening at the ice-bed interface due to rapid injection of melt-water, whereas opening of the through-ice vertical crack was the principal contributor to the horizontal surface displacements²³. Similar observations have since been made at other west Greenland Ice Sheet supraglacial lakes^{2,3} all providing definitive evidence for rapid melt-water drainage to the bed during hydrofracture events.

A limitation of these prior studies was insufficiently dense observations of surface motion required to directly constrain the mechanism and location of hydro-fracture initiation and the

spatial distribution of melt-water at the ice-sheet bed. Here we present results from a spatially-dense array of 16 GPS stations positioned around North Lake between 2011 and 2013 (Fig. 1). This array captured the dynamic response of the ice sheet to rapid lake drainages in each of the three years of the study, allowing us to infer the evolving hydro-fracture geometry and spatial distribution of melt-water at the ice-sheet bed before, during, and after drainages.

From these GPS data, we identify a period of precursory ice motion, indicative of the presence of an increased volume of water reaching the bed within the GPS array, hours before each year's local hydro-fracture initiation and rapid lake drainage (Extended Data Table 1). The displacement anomalies (Figs. 2a–c) show the along-flowline, crack-normal, and vertical displacement histories for two days prior to and one day following each drainage event at stations NL08 and NL01 or NL03 (Fig. 1, Methods). We pick three time points for each drainage (using all available stations) that designate the start of the precursor, hydro-fracture initiation, and the maximum hydro-fracture opening (Fig. 2; Extended Data Table 1).

The 2011 precursor is manifested as vertical uplift followed by increased displacement in the flow-line direction at stations southwest of moulin M1 (NL07, NL08, NL10) over the 10 hours leading up to rapid lake drainage (Figs. 1, 2a, 3a). This is consistent with field observations that suggest as North Lake filled over the preceding days the western shoreline reached M1, allowing melt-water to begin pooling in and reactivating M1 prior to lake drainage, thus permitting increased basal slip (Extended Data Figs. 1, 2). Similarly, we observe increased displacement in the flow-line direction prior to the 2012 and 2013 hydro-fracture events, which we also interpret to be hydrologically induced (Fig. 2b, c) (Supplementary Discussion in

Methods). In 2012 the precursor is manifested as anomalous along-flowline displacements at stations in the northern end of the array (e.g., NL01 and NL02), but shows little signal at the southern stations (Extended Data Fig. 4a). The 2013 precursor is manifested as enhanced flowline displacements at all western stations (FL03, NL04, NL07, NL08, NL10), as well as vertical uplift focused just west of the lake basin (Extended Data Fig. 5a). All three precursors have similar durations (6–12 hours), but they occur in different subsets of the spatial array. Following each precursor there is clear evidence of the main 4-km long hydro-fracture opening and subsequent rapid lake drainage, as indicated by the ~3 hour long, 5–10 cm excursion of NL08 in the crack-normal (southward) direction, which is rapidly recovered due to closing of the fracture (Figs. 2a–c). In all three years the hydro-fracture opening phase is accompanied by considerable (>20 cm) uplift and enhanced along-flowline motion across many stations in the network.

To quantitatively constrain the processes responsible for these surface motions, we exploit the high spatial density of our GPS data to invert for the space-time history of deformation surrounding the lake drainages. We use the Network Inversion Filter (NIF) algorithm²⁴ to model the GPS time series of drainage-related surface motion as the summation of three deformation sources: (1) hydro-fracture opening, (2) basal cavity opening (due to the rapid injection of melt-water), and (3) extra basal slip above the background rate (due to enhanced basal lubrication) (Methods) (Extended Data Figs. 6–8). The NIF utilizes Green’s functions for an elastic half-space to relate the surface displacement time series to the space-time history of opening and slip along prescribed planes describing each of these deformation sources²⁴ (Methods).

123

124 The NIF results provide estimates of the spatial distribution of melt-water at the ice-sheet
125 bed before, during, and after drainages. Full inversion results for the 2011–2013 drainages are
126 presented as movies (Supplementary Information Movies 1–3). Figures 2d–f show spatially
127 integrated results from 2011–2013 for the three deformation sources: hydro-fracture crack
128 volume, basal cavity volume, and basal slip (shown as moment M_0 ; see Methods). For the 2011
129 event, we identify basal cavity opening and slip associated with the precursor southeast and
130 southwest of M1, respectively, before the hydro-fracture opens (Figs. 2d, 3a–c)—indicating the
131 injection of melt-water at the ice-sheet bed prior to local hydro-fracture initiation. Immediately
132 following the precursor, the hydro-fracture opens first at M1, and then propagates east beneath
133 the basin (Supplementary Information Movie 1). At the time of maximum hydro-fracture
134 opening (Fig. 3d–f), the basal cavity volume (Figs. 2d) is nearly equivalent to the North Lake
135 pre-drainage volume estimate of $0.007 \pm 0.001 \text{ km}^3$ (Methods) (Extended Data Table 1;
136 Extended Data Figs. 2, 3). The agreement between lake volume calculations and NIF estimates
137 of basal cavity volume validates our inversion results. Basal slip is focused within, and a few km
138 south of, the lake basin, but not northward possibly due to a known ridge in the basal topography
139 (Fig. 3d)^{5,25}.

140

141 Inversion results for the rapid drainage events in 2012 and 2013 also suggest precursory
142 activity (Supplementary Discussion). The 2012 precursor is associated with basal slip 3 km
143 north of the hydro-fracture, possibly due to enhanced lubrication from nearby melt-water input to
144 the bed (Extended Data Fig. 4a). The 2013 precursor was the most extensive, producing
145 enhanced basal slip over a $5 \times 5 \text{ km}$ area as well as significant basal uplift (Extended Data Fig.

5a,b). In both 2012 and 2013, the hydro-fracture opening and lake drainage produce ~50 cm of basal cavity opening beneath the lake basin and enhanced basal slip over a wide area (Extended Data Figs. 4d–f & 5d–f).

Previous work on the 2006 North Lake drainage event identified a slow steady drop in lake level in the 16 hours prior to the rapid hydro-fracture induced drainage, and it was hypothesized that this pre-drainage may have been due to the initial filling of a slowly propagating hydro-fracture directly beneath the lake basin, or water over-spilling into an adjacent crack system¹. However, the observations in 2006 were insufficient to distinguish between these (or alternative) mechanisms. Our NIF results show no evidence for the slow downward propagation of a hydro-fracture prior to lake drainage, which would be manifest as crack-normal horizontal displacements. Rather, the inversions clearly demonstrate that each drainage is preceded by a period of enhanced basal slip and/or uplift, that is likely caused by the injection of melt-water at the bed via neighboring hydro-fractures and moulins. Intriguingly, precursor motion was also observed prior to other lake drainages^{1,2}, though it was not identified as a triggering mechanism for hydro-fracture initiation (Supplemental Discussion). The observation of a precursor before rapid lake drainages strongly suggests that they play an important role in triggering hydro-fractures, possibly by inducing local stress perturbations that overcome the background compressive stresses found in lake basins^{5,26}.

To test the hypothesis that local stress perturbations play an important role in triggering hydro-fractures, we compared the background viscous stresses in the lake basin to the elastic stress change induced by the precursory basal slip and cavity opening (Methods). We calculated

background compressive stresses of order -70 ± 40 kPa within the lake basin, comparable to other west Greenland lake basin estimates²⁶. Prior to the start of the precursor, changes in crack-normal stress ($\Delta\sigma_n$) on the hydro-fracture are $\Delta\sigma_n = 0 \pm 40$ kPa. However, throughout the precursor $\Delta\sigma_n$ increases, attaining maxima tensile stresses of +100 to +600 kPa at the top of the hydro-fracture at the onset of rapid drainage (Fig. 4 a–c). These calculations confirm that the drainage precursors can generate tensile crack-normal stresses near the surface with sufficient magnitude to temporarily overcome the compressive background stress and promote hydro-fracture initiation.

Our results and reinterpretation of previous studies (Supplemental Discussion) indicate that injection of surface melt-water, routed from supraglacial lakes to the bed through pre-existing crevasses or conduits, is required to trigger hydro-fracture initiation and subsequent rapid lake drainage in an otherwise compressional basin. As shown previously, a necessary condition for hydro-fracture propagation is a sufficient volume of water to keep the fracture filled^{7,9}. Lacking a known triggering mechanism, prior studies used only this volume threshold to predict that lake drainages would occur^{14,27,28}. However, we do not find that lakes spontaneously hydro-fracture once they surpass this threshold¹². In all 3 years, North Lake contained $\sim 5\times$ the critical volume of water necessary to keep a 4 km long crack open to the bed (Methods) before hydro-fracture occurred. Thus, we argue against the exclusive use of a volume threshold for triggering supraglacial lake drainage in regional ice sheet modeling studies.

We hypothesize that if stress transients associated with enhanced melt-water transport to the bed beneath lakes are required to initiate surface-to-bed hydro-fractures in compressional

lake basins, then lakes are less likely to create large-scale hydro-fractures in interior regions of the Greenland Ice Sheet where melt-water access to the bed is limited by lack of pre-existing crevasses^{5,14–16,29}. As new lakes form at higher elevations in a warming climate^{10–14} they will encounter longer wavelength surface topography^{5,30,31}, resulting in greater distances between compressive lake basins and extensional crevasse-forming regions. Thus, lake water must be routed greater distances in surface streams down the ice sheet before encountering crevasses where through-ice drainage conduits can be established, minimizing local stress transients and potentially obstructing *in situ* rapid drainage of high elevation lakes and the formation of new surface-to-bed hydro-fractures beneath lake basins²⁹. This indicates that while lake drainages may be important for inland expansion of enhanced flow at mid-elevations¹⁶, such expansions are more likely influenced by longitudinal coupling at high elevations³² (see Supplementary Discussion). Finally, the supply of melt-water to the bed may not be well correlated with the location, abundance, and size of high elevation supraglacial lakes.

References and Notes:

1. Das, S. B. *et al.* Fracture Propagation to the Base of the Greenland Ice Sheet During Supraglacial Lake Drainage. *Science*. **320**, 778–781 (2008).
2. Doyle, S. H. *et al.* Ice tectonic deformation during the rapid in situ drainage of a supraglacial lake on the Greenland Ice Sheet. *Cryosph.* **7**, 129–140 (2013).
3. Tedesco, M. *et al.* Ice dynamic response to two modes of surface lake drainage on the Greenland ice sheet. *Environ. Res. Lett.* **8**, 34007 (2013).
4. Joughin, I. *et al.* Seasonal Speedup Along the Western Flank of the Greenland Ice Sheet. *Science*. **320**, 781–783 (2008).
5. Joughin, I. *et al.* Influence of ice-sheet geometry and supraglacial lakes on seasonal ice-flow variability. *Cryosph.* **7**, 1185–1192 (2013).
6. Andrews, L. C. *et al.* Direct observations of evolving subglacial drainage beneath the Greenland Ice Sheet. *Nature* **514**, 80–83 (2014).
7. Krawczynski, M. J., Behn, M. D., Das, S. B. & Joughin, I. Constraints on the lake volume required for hydro-fracture through ice sheets. *Geophys. Res. Lett.* **36**, L10501 (2009).
8. Weertman, J. Can a water filled crevasse reach the bottom surface of a glacier? *IASH Publ.* **95**, 139–145 (1973).
9. Van Der Veen, C. J. Fracture propagation as means of rapidly transferring surface meltwater to the base of glaciers. *Geophys. Res. Lett.* **34**, L01501 (2007).
10. Sundal, A. V. *et al.* Evolution of supra-glacial lakes across the Greenland Ice Sheet. *Remote Sens. Environ.* **113**, 2164–2171 (2009).
11. Howat, I. M., de la Peña, S., van Angelen, J. H., Lenaerts, J. T. M. & van den Broeke, M. R. *Brief Communication* “Expansion of meltwater lakes on the Greenland Ice Sheet.” *Cryosph.* **7**, 201–204 (2013).
12. Fitzpatrick, A. A. W. *et al.* A decade (2002–2012) of supraglacial lake volume estimates across Russell Glacier, West Greenland. *Cryosph.* **8**, 107–121 (2014).
13. Parizek, B. R. & Alley, R. B. Implications of increased Greenland surface melt under global-warming scenarios: ice-sheet simulations. *Quat. Sci. Rev.* **23**, 1013–1027 (2004).
14. Leeson, A. A. *et al.* Supraglacial lakes on the Greenland ice sheet advance inland under warming climate. *Nat. Clim. Chang.* **5**, 51–55 (2015).

- 235 15. Bartholomew, I. D. *et al.* Seasonal variations in Greenland Ice Sheet motion: Inland extent
236 and behaviour at higher elevations. *Earth Planet. Sci. Lett.* **307**, 271–278 (2011).
- 237 16. Doyle, S. H. *et al.* Persistent flow acceleration within the interior of the Greenland ice
238 sheet. *Geophys. Res. Lett.* **41**, 899–905 (2014).
- 239 17. Zwally, H. J. *et al.* Surface melt-induced acceleration of Greenland ice-sheet flow. *Science*
240 **297**, 218–222 (2002).
- 241 18. Bartholomew, I. *et al.* Short-term variability in Greenland Ice Sheet motion forced by
242 time-varying meltwater drainage: Implications for the relationship between subglacial
243 drainage system behavior and ice velocity. *J. Geophys. Res.* **117**, F03002 (2012).
- 244 19. Hoffman, M. J., Catania, G. a., Neumann, T. a., Andrews, L. C. & Rumrill, J. a. Links
245 between acceleration, melting, and supraglacial lake drainage of the western Greenland
246 Ice Sheet. *J. Geophys. Res.* **116**, F04035 (2011).
- 247 20. Selmes, N., Murray, T. & James, T. D. Fast draining lakes on the Greenland Ice Sheet.
248 *Geophys. Res. Lett.* **38**, 1–5 (2011).
- 249 21. Smith, L. C. *et al.* Efficient meltwater drainage through supraglacial streams and rivers on
250 the southwest Greenland ice sheet. *Proc. Natl. Acad. Sci.* **112**, 1001–1006 (2015).
- 251 22. Pimentel, S. & Flowers, G. E. A numerical study of hydrologically driven glacier
252 dynamics and subglacial flooding. *Proc. R. Soc. A Math. Phys. Eng. Sci.* **467**, 537–558
253 (2010).
- 254 23. Tsai, V. C. & Rice, J. R. A model for turbulent hydraulic fracture and application to crack
255 propagation at glacier beds. *J. Geophys. Res.* **115**, F03007 (2010).
- 256 24. Segall, P. & Matthews, M. Time dependent inversion of geodetic data. *J. Geophys. Res.*
257 **102**, 22391–22409 (1997).
- 258 25. Bamber, J. L. *et al.* A new bed elevation dataset for Greenland. *Cryosph.* **7**, 499–510
259 (2013).
- 260 26. Catania, G. A., Neumann, T. A. & Price, S. F. Characterizing englacial drainage in the
261 ablation zone of the Greenland ice sheet. *J. Glaciol.* **54**, 567–578 (2008).
- 262 27. Clason, C., Mair, D. W. F., Burgess, D. O. & Nienow, P. W. Modelling the delivery of
263 supraglacial meltwater to the ice/bed interface: application to southwest Devon Ice Cap,
264 Nunavut, Canada. *J. Glaciol.* **58**, 361–374 (2012).
- 265 28. Arnold, N. S., Banwell, a. F. & Willis, I. C. High-resolution modelling of the seasonal
266 evolution of surface water storage on the Greenland Ice Sheet. *Cryosph.* **8**, 1149–1160
267 (2014).

- 268 29. Poinar, K. *et al.* Limits to future expansion of surface-melt-enhanced ice flow into the
269 interior of western Greenland. *Geophys. Res. Lett.* (2015). doi:10.1002/2015GL063192
- 270 30. Sergienko, O. V. Glaciological twins: basally controlled subglacial and supraglacial lakes.
271 *J. Glaciol.* **59**, 3–8 (2013).
- 272 31. Lampkin, D. J. & VanderBerg, J. A preliminary investigation of the influence of basal and
273 surface topography on supraglacial lake distribution near Jakobshavn Isbrae, western
274 Greenland. *Hydrol. Process.* **25**, 3347–3355 (2011).
- 275 32. Price, S. F., Payne, A. J., Catania, G. A. & Neumann, T. A. Seasonal acceleration of
276 inland ice via longitudinal coupling to marginal ice. *J. Glaciol.* **54**, 213–219 (2008).

277

278 **Supplementary information is available in the online version of the paper.**

279 **Acknowledgments:** Support was provided by the National Science Foundation's Office of Polar
280 Programs (NSF-OPP) and National Aeronautics and Space Administration's (NASA)
281 Cryospheric Sciences Program through ARC-0520077, ARC-1023364, and
282 NNX10AI30G to S.B.D. and M.D.B., and through ARC-0520382, ARC-1023382, and
283 NNX10AI33G to I.J.. WorldView image data used for this work was provided by the
284 Polar Geospatial Center at the University of Minnesota with support from NSF grant
285 ANT-1043681. L.A.S. was also supported by a National Science Foundation Graduate
286 Research Fellowship. Logistical and instrumental support was provided by UNAVCO,
287 PASSCAL, and CH2MHILL Polar Field Services.

288 **Author Contributions:** M.D.B., S.B.D., and I.J. conceived the study. L.A.S., M.D.B., S.B.D.,
289 I.J., and D.S. carried out the fieldwork. L.A.S., T.H., and M.K. processed and analyzed the
290 GPS data. J.J.M. and L.A.S. developed the Network Inversion Filter. D.S. created the
291 Digital Elevation Models. L.A.S., M.D.B., S.B.D., I.J., and J.J.M. interpreted the results.
292 L.A.S. wrote the paper. All authors commented on the paper.

293

294 **Author Information:** The authors declare no competing financial interests. Correspondence and
295 requests for materials should be addressed to L.A.S. (stevensl@mit.edu).
296

297 **Main Text Figure Legends:**

298 **Fig. 1. June 17, 2011 Synthetic Aperture Radar (SAR) image showing the extent of North**
299 **Lake (center) and surrounding lakes one day before the 2011 rapid North Lake drainage.**
300 Yellow triangles show GPS locations. The M1 moulin is also shown.

301 **Fig. 2. 2011, 2012, and 2013 North Lake Drainages.** GPS station displacement less
302 background velocities shown in solid (dashed) lines for station NL08 (NL01 or NL03) flowline
303 displacement (blue), crack-normal displacement (black), and relative vertical uplift (red) over the
304 two days prior and one day following the (a) 2011, (b) 2012, (c) 2013 drainage events. The
305 bottom row shows NIF-derived hydro-fracture opening volume (black), basal cavity opening
306 volume (red), and basal slip moment (blue) across the domain for the two days prior to and one
307 day following the (d) 2011, (e) 2012, (f) 2013 drainage events. The coordinate system is
308 orientated such that hydro-fracture opening is expressed primarily in the horizontal crack-normal
309 component, while basal slip is primarily expressed in the horizontal flowline component, and
310 basal cavity opening is primarily reflected in the vertical component data. The precursor and
311 rapid lake drainage periods are designated by three time points across the drainages: (1) the start
312 of the precursor at the time of first distinguishable deviation of station vertical uplift, crack-
313 normal, or flowline displacement from the background velocity field (“1. Start of Precursor”);
314 (2) hydro-fracture initiation at the time of maximum NL08 southward crack-normal acceleration
315 (“2. H-F Initiation”); and, (3) the maximum hydro-fracture opening at the time of maximum
316 southward NL08 crack-normal displacement (“3. Max H-F Opening”) (Extended Data Table 1).

317
318 **Fig. 3. 2011 Basal slip and cavity opening at hydro-fracture initiation and maximum hydro-**
319 **fracture opening.** NIF-calculated (a) extra basal slip accumulated, (b) basal cavity opening, and
320 (c) hydro-fracture crack opening at the time of the 2011 (a–c) hydro-fracture initiation and (d–f)
321 maximum hydro-fracture opening (time points shown in Fig. 2a). Moulin location, last known
322 lake shoreline, GPS stations, and NIF vertical crack surface trace derived from SAR imagery are
323 shown as a yellow circle, blue line, black triangles, and black line, respectively. Vector fields
324 show GPS (NIF) displacement less background velocities in black (green) for (a) the period
325 between the start of the precursor and hydro-fracture initiation, and (d) the period between
326 hydro-fracture initiation and maximum hydro-fracture opening. Error ellipses of 1 sigma are
327 shown for the GPS displacements (blue ellipses). Basal subelements are 0.83 km by 0.83 km,
328 resulting in 144 subelements over a 10 km by 10 km region.

329
330 **Fig. 4 Change in Crack-normal Stress during the Precursor.** Changes in the crack-normal
331 elastic stresses ($\Delta\sigma_n$) (kPa) (compressive = negative; tensile = positive) on the hydro-fracture
332 crack as a result of basal cavity opening and accumulated extra basal slip during the (a) 2011, (b)
333 2012, and (c) 2013 precursor. Stresses are calculated at the start of the precursor and hydro-
334 fracture initiation, coinciding with the times noted in Extended Data Table 1, and then
335 differenced to show the change in elastic stress that occurs during the precursor.

Methods:

- 1. GPS Data.**
- 2. Lake Volume.**
- 3. Network Inversion Filter.**
- 4. Basal Moment Calculations.**
- 5. Critical Volume for Driving Water-filled Hydro-fracture to Bed.**
- 6. North Lake basin Stresses.**
- 7. Data.**

Supplementary Discussion

- 1. Precursors Observed in Previous Studies.**
- 2. Implications for Inland Expansion of Seasonal Acceleration.**
- 3. 2012 North Lake Drainage.**
- 4. 2013 North Lake Drainage.**

1. GPS Data.

Continuous 30-s resolution GPS data collected by dual-frequency Trimble NetR9 receivers were processed with Track software³³. GPS data for each station were processed individually relative to the 30-s resolution Greenland GPS Network (GNET) KAGA base station located on bedrock ~55 km from North Lake³⁴. The 30-s resolution position estimates and corresponding uncertainties from Track were used in the NIF and plotted in Extended Data Figures 6, 7, and Supplementary Information Movies 1–3. For plotting purposes, the data in Figure 2 were smoothed over a 2-minute window with a five-point central moving average. Error output from Track software is given as 1-sigma errors for East, North, and Up offsets from the coordinates of the first position in the time series, but not the full covariance matrix³³. Horizontal (vertical) 1-sigma errors are consistently ± 2 cm (± 5 cm) across all stations and years.

Of the 16 GPS stations in the North Lake array, stations NL08, NL01 and/or NL03 best capture differences between the precursors over the three drainage events (Fig. 2). NL08 is consistently the most responsive station during lake drainage events, and proves to be the best single station indicator of the drainage event as a whole. NL08 captures the 2011 and 2013

precursor well (Fig. 2 a & c). In 2012, the precursor is manifested as anomalous along-flowline displacements observed at stations NL01 and NL02. Thus, we show of these northern stations (NL01) alongside the NL08 timeseries to show the along flowline speed up in the northern portion of the array during the 2012 precursor (Fig. 2b). In 2013, NL01 and NL02 stations were not recording during the drainage, leaving NL03 as the closest station in the northern portion of the array to NL01/NL02 (Fig. 2c). Lake drainage duration is calculated based on NL08 crack-normal motion from the start of the hydro-fracture opening to when NL08 crack-normal motion regains its southward displacement as the crack closes ($\sim 1\text{--}2$ hours after time of maximum hydro-fracture opening) (Fig. 2, Extended Data Table 1).

Lake Volume.

The NASA Ames Stereo Pipeline³⁵ stereographic software was used to generate ~ 2 m per pixel digital elevation models (DEMs) of the empty, post-drainage North Lake basin using a WorldView-1 stereopair acquired on 7/21/2011 and a WorldView-2 stereopair acquired on 7/5/2013 (Extended Data Fig. 2). Orthorectified ~ 0.5 m per pixel WorldView images depicting the last available pre-drainage North Lake shoreline were used to constrain the lake shoreline position and thus, lake depth and volume from the DEM. The 2011 lower bound on the lake volume estimate for North Lake was calculated from the shoreline position on a 6/17/2011 WorldView-1 image obtained 1 day before the 2011 drainage. The 2013 lower bound for lake volume for North Lake was calculated from the shoreline position on a 6/17/2013 WorldView-2 image obtained 2 days before the 2013 drainage. While small-scale surface features (moulins, supraglacial stream channels) advect ~ 100 m yr^{-1} to the WNW, the North Lake basin geometry is the result of fixed bed topography, and does not change significantly between summers (Extended Data Fig. 3). Lake volume estimates are given in Extended Data Table 1.

In 2012, a lack of satellite images of North Lake basin during the days leading up to drainage prevented lake volume calculation via shoreline position and DEM methods. Output from the Regional Atmospheric Climate Model for the Greenland Ice Sheet (RACMO2/GR)³⁶ for 2011 and 2012 was used to compare estimated cumulated runoff in the North Lake region (68.66°N, -49.52°W) at the day of lake drainage between the two years. We found that RACMO2/GR values of cumulative runoff at DOY 169 2011 and DOY 161 2012 are very similar at 0.0030 kg m⁻² and 0.0031 kg m⁻², respectively. Average daily runoff values at this location during mid-June are on the order 0.0003 kg m⁻² day⁻¹. Thus, we conclude the pre-drainage 2012 North Lake volume is on the order of the pre-drainage 2011 NL volume: 0.007 ± 0.001 km³. We hypothesize that the pre-drainage 2012 North Lake shoreline reached M1 at the time of drainage.

3. Network Inversion Filter.

We implemented the Network Inversion Filter (NIF) algorithm²⁴ to determine the amount of opening along a vertical crack and slip and opening along a basal crack during the 2011, 2012, and 2013 North Lake rapid drainage events. The NIF utilizes Green's functions for an elastic half-space³⁷ to relate surface displacement time series to the space-time history of opening and slip along prescribed planes²⁴. The North Lake basin is modeled using an isotropic elastic half-space with the GPS stations at the surface. Three deformation sources are included: (1) hydro-fracture opening, (2) basal cavity opening (due to the rapid injection of melt-water), and (3) extra basal slip above the background rate (due to enhanced basal lubrication). The NIF assumes linear elastic behavior for the ice sheet, and treats hydro-fracture as a horizontal elastic dislocation along a vertical crack within the ice⁸. These assumptions are justified by vertical-

crack propagation timescales (seconds to minutes) that are shorter than the Maxwell time of ice (6 to 24 hours)^{7,9,22,23}.

We model the GPS position vector \mathbf{X} for each GPS station i , as a function of time t relative to the starting time t_0 as follows^{24,38}:

$$\mathbf{X}_i(t) - \mathbf{X}_i(t_0) - \mathbf{V}_i(t - t_0) = \mathbf{G}_i \mathbf{s}(t) + \mathbf{L}_i(t) + \mathbf{F} \mathbf{f}(t) + \boldsymbol{\varepsilon}(t) \quad (1)$$

where the left hand side represents the drainage-related surface motion of the GPS stations obtained by removing the station background velocity field³⁸ \mathbf{V} . \mathbf{V} is determined for each station by calculating station velocity over the 2 days of data available prior to the start of the precursor. On the right hand side of Equation (1), \mathbf{G} represents the matrix of elastic Green's functions³⁷, $\mathbf{s}(t)$ is a vector of slip (or opening) on each deformation plane subfault at time t , $\mathbf{L}_i(t)$ is component specific colored noise, $\mathbf{F}\mathbf{f}(t)$ represents reference frame errors³⁸ at time t , and $\boldsymbol{\varepsilon}(t)$ represents normally distributed white noise observation error at time t . We model $\mathbf{L}(t)$ with a Brownian random walk model as has been done in previous studies of high-rate GPS data³⁹. This term is necessary to absorb colored noise in the time series due to unmodeled errors in the position estimates and possibly local benchmark instabilities. The random walk is described by a scale parameter τ , which we estimated to be $5 \text{ cm day}^{-1/2}$ by modeling data prior to the start of the precursor as a combination of a background velocity and random walk ($5 \text{ cm day}^{-1/2}$ was the smallest value that resulted in white residuals for such a model). We use three perpendicular translations for $\mathbf{F}\mathbf{f}(t)$ due to the small size of our network³⁸. The data vector in the Kalman filter is given by the GPS position data $\mathbf{X}_i(t)$ minus the background velocity ($\mathbf{D}_i(t) = \mathbf{X}_i(t) - \mathbf{X}_i(t_0) - \mathbf{V}_i(t - t_0)$). The data covariance matrix is assumed to be diagonal and derived from the individual

component errors from the Track processing modified appropriately given the uncertainty in our estimate of \mathbf{V} ³⁸.

The vertical plane for the hydro-fracture extends from 100 to 1100 m depth striking along the surface expression of the most substantial recurring hydro-fracture crack intersecting M1 on the western edge of the lake basin (Extended Data Fig. 1). The vertical plane does not start at the surface of the elastic half-space because the Green's Functions used in the NIF algorithm are for dislocations within the halfspace³⁷. This approximation is sufficient because the vertical crack is located within the lake and our GPS stations are located >1km outside the lake basin and thus, are not sensitive to the shallowest 100 m of crack opening. On the vertical plane we solve only for mode-I tensile motion corresponding to opening of the crack⁴⁰. The vertical plane is subdivided into 24 subfaults along strike and 6 subfaults along dip; each vertical subfault is 0.19 km wide and 0.16 km tall.

The basal plane is defined as a 100-km² sub-horizontal plane at 1100 m depth, dipping 0.01° to the west, and centered beneath the North Lake basin (68.723 N, -49.53 W). The basal plane strikes 186 degrees from North, perpendicular to the direction of average ice velocity as determined from the average of all GPS stations' velocity in the days leading up to each year's drainage event. We estimate both mode-I tensile and dip-slip motion in the direction of ice flow on the basal plane. The basal plane is subdivided into 12 subfaults along dip and 12 subfaults along strike; each subfault is a 0.83×0.83 km square. The shallow depth of the basal plane within the half-space results in Green's function magnitudes above 0.95 for the uplift response at GPS stations to basal plane opening. Therefore, we neglect the material property contrast at the ice

sheet–bedrock interface in our model because it would only modify the Green’s function magnitude by a few percent³⁷. The geometry of our array, with a 10:1 ratio of horizontal distance across the GPS array to ice thickness, allows us to resolve slip and opening on the basal plane on the length scale of the station spacing (1–3 km).

Our choice of a nearly horizontal basal plane is motivated by the presence of a relatively flat basin in the bedrock topography centered directly beneath North Lake^{5,25}, which yields a nearly horizontal basal slope across the entire GPS array. Moreover, sensitivity tests show that our NIF results are robust for basal plane dips up to 5°. This value is greater than the maximum bedrock slope (3.4°) measured from the bedrock basin center beneath North Lake to the bedrock ridge 5 km to the west of the lake basin^{5,25}. Thus, we find no reason to add complexity associated with small variations in basal topography and/or to correct the GPS displacements for the vertical distance gained as the stations move up and out of the basin.

We used a Maximum likelihood estimation (MLE) algorithm to determine appropriate ranges of values for the spatial (γ) and temporal (α) hyperparameters for both the vertical and basal planes²⁴. We determined the final hyperparameter values based on a combination of MLE estimates and analysis of NIF output to identify hyperparameter values low enough to provide significant model smoothing, but high enough to still track station displacements during the few hours of rapid drainage in the timeseries. The MLE estimates provide an average value that is appropriate over the entire time series, but therefore, oversmooths the time periods of rapid deformation when higher values of α and γ are warranted by the data. The MLE calculations of the vertical-plane temporal hyperparameter suggest values of α of 100 (2011), 200 (2012), and

1000 (2013); however, slightly higher or lower α values of 150 (2011), 250 (2012), and 500 (2013) were used based on NIF ability to track station displacements during the rapid drainage (Extended Data Fig. 8). The vertical-plane spatial smoothing parameter, γ , could not be constrained based on MLE calculations. The MLE calculations suggest a higher than necessary value of the spatial hyperparameter for the vertical crack, resulting in unrealistic vertical plane opening and closing on spatial scales of <0.5 km along strike. Therefore, we set the vertical plane spatial parameter to $\gamma=450$ for the 2011 and 2012 inversions, resulting in vertical plane opening and closing on scales of 1 km along strike.

The basal plane spatial and temporal hyperparameters were also not satisfactorily constrained by MLE calculations for 2011 and 2012. The MLE calculations recommended higher than necessary spatial and temporal hyperparameters, resulting in unrealistic, over-fit solutions for the basal plane. The chosen basal plane temporal parameter ($\alpha = 25$) is substantially lower than the temporal parameter of the vertical plane, resulting in a smoother solution of bed opening and slip. The chosen basal plane spatial parameter ($\gamma = 50$) resolves basal slip and opening on spatial scales of 2 km, consistent with our 1 to 3 km GPS station spacing on the ice-sheet surface (Fig. 1). For 2013, the rapid oscillatory variations in the crack-normal component of displacement (North) for several stations required a larger basal-plane spatial parameter ($\gamma=500$) in order to allow the migration of sufficiently compact slip patches required to fit the oscillations in the crack-normal data (Supplementary Discussion: 2013 North Lake Drainage).

4. Basal Moment Calculations.

Basal slip moment M_0 , in N·m, is calculated to provide an integrated measure of slip across the basal plane:

$$M_0 = \mu AD \quad (3)$$

where μ , the shear modulus for glacial ice, is taken to be 3.5 GPa⁴¹, A is the area of the basal plane in square meters, and D is the mean bed slip across the basal plane just after drainage in meters (Extended Data Table 1). Moment magnitude (M_w) is calculated from the basal slip moment⁴²: $M_w = (2/3)\log(M_0) - 6.05$ (Extended Data Table 1).

5. Critical Volume for Driving Water-filled Hydro-fracture to Bed.

The critical volume of water necessary to keep a 4 km long crack open to the bed ranges from 0.0008 to 0.0020 km³. This estimate is derived based on a mean crack opening of 0.2–0.5 m required to drive a 4 km long, 100% water-filled vertical crack through 1 km of glacial ice with a shear modulus of 1.5–3.9 GPa⁷.

6. North Lake Basin Stresses.

To calculate background viscous stresses in North Lake basin, we use Glen's flow law⁴³ to convert longitudinal (along flow) surface strain rates derived from TerraSAR-X 2009–2011 winter velocity measurements⁵ to longitudinal stresses, σ_{jk} :

$$\sigma_{jk} = A^{-[1/n]} \dot{\epsilon}_E^{[1-n]/n} \dot{\epsilon}_{jk} \quad (2)$$

where the creep parameter, A , is $3.5 \times 10^{-25} \text{ s}^{-1} \text{ Pa}^{-3}$ ⁴⁴, $n=3$ is the creep exponent, $\dot{\epsilon}_E$ is the two-dimensional effective strain rate, and $\dot{\epsilon}_{jk}$ is longitudinal strain rate. We use the same Green's functions from the NIF³⁷ to calculate the change in crack-normal stress ($\Delta\sigma_n$) on the hydro-fracture that was induced by the basal cavity opening and accumulated extra basal slip during the two days leading up to each drainage event.

532

533 **7. Data.**

534 Source data for all figures and movies are available online as Excel spreadsheets.

Supplementary Discussion:

1. Precursors Observed in Previous Studies.

While our study is the first to interpret the cause and significance of precursors to rapid lake drainage, similar precursors have been observed prior to other recorded rapid supraglacial lake drainages on the western margin of the Greenland Ice Sheet in the form of GPS station uplift and steady lake level lowering in the hours before hydro-fracture^{1,2}. During a rapid North Lake drainage in 2006, NLBS GPS station uplift and steady lake level lowering was observed prior to rapid lake level drop and northward ice motion indicative of hydro-fracture opening¹. Slow lake level lowering was also observed before a 2008 rapid drainage of South Lake (68.58 N, 49.39 W), another lake site in this region located 20 km south of North Lake⁵. During the rapid drainage of Lake F (67.01 N, 48.74 W) in 2010, uplift of two GPS stations on the eastern side of the lake is observed over the 7 hours leading up to rapid drainage². Precursory motion was not observed during the rapid drainage of Lake Ponting in 2011 (69.57 N, 49.81 W); however, the four GPS stations used to record ice motion may have been located too far from the lake to record precursory motion³. The three rapid drainage precursors observed during 2011–2013 at North Lake allow us to reinterpret precursors of past rapid lake drainages as evidence of a hydrologically-induced trigger for hydro-fracture. Further, our results provide a possible mechanism by which a lake drainage could generate a melt-water pulse that could trigger additional lake drainages in the vicinity. Such regionally clustered lake drainages have been noted in previous lake drainage studies^{2,12}.

2. Implications for Inland Expansion of Seasonal Acceleration.

The formation and drainage of high elevation lakes has been invoked to explain the inland expansion of seasonal acceleration (enhanced summer velocities up to 8% above winter velocities) during high melt summers now¹⁶ and in the future¹⁴. The precursors observed here suggest enhanced melt-water transport to the bed beneath lakes is needed to generate tensile stress transients that promote the initiation of surface-to-bed hydro-fractures. For this proposed hydro-fracture initiation mechanism, there must exist both a sufficient reservoir of surface melt-water and a nearby surface-to-bed pathway to transport the melt-water to the bed beneath the lake. Our results inform our hypothesis that rapid lake drainages are unlikely to progress inland to areas of new surface melting based on the overall decline in tensile strain rates towards the ice sheet interior, which results in increasingly rare crevasses with elevation²⁹. Thus, much of the new surface melt in the interior likely drains via long (10s of km) supraglacial streams that eventually terminate in moulins in regions where surface melt-water already reaches the bed at present²⁹. While surface melt may continue to expand inland, much of this melt-water will only reach the bed in areas further downstream where seasonal lubrication already occurs^{15,19,29}. An alternative explanation for the observed seasonal acceleration is longitudinal coupling of these higher elevations (above ~1600 m a.s.l.) to lower elevation regions (below ~1600 m a.s.l.) that are responding to increased melt input^{45,32,46}.

3. 2012 North Lake Drainage.

In 2012, North Lake drained rapidly over a period of ~5 hours beginning at 22:12 local time on June 9, 2012 (DOY 161). Due to the lack of satellite images bracketing the North Lake drainage window, the maximum volume of North Lake in 2012 is unknown prior to drainage. Using RACMO runoff estimates, we conclude that the 2012 North Lake volume was similar to

the 2011 volume based on a difference of $+0.00012 \text{ kg/m}^2$ of cumulative runoff between the two years (Methods: Lake Volume).

Regional basal slip prior to the 2012 North Lake hydro-fracture initiation indicates the presence of increased basal melt-water at the ice-sheet bed prior to North Lake hydro-fracture. Over the 16 hours leading up to North Lake hydro-fracture initiation, stations NL01 and NL02 experience an additional 5 cm of flowline-parallel displacement (Figs. 2b; Extended Data Fig. 4a). At the end of the precursor, slip in the northern portion of the array results in a basal moment (M_0) of 10^7 N m (Figs. 2e; Extended Data Fig. 4a), though there is minimal basal cavity opening throughout the array (Extended Data Fig. 4b). Over the following 3.5 hours, the hydro-fracture opens beneath the North Lake basin, reaching its maximum width 2.5 hours after hydro-fracture initiation. As in the 2011 North Lake rapid drainage, basal cavity opening is centered beneath and to the south of the North Lake basin during the 2012 drainage (Extended Data Fig. 4e; Movie 2). During lake drainage, basal slip beneath and to the southwest of the North Lake basin occurs, while the basal slip initially accumulated to the north during the precursor (Extended Data Fig. 4a) remains and expands south (Extended Data Fig. 4d).

4. 2013 North Lake Drainage.

In 2013, GPS station attrition in the eastern half of the array precludes various array-scale NIF conclusions; however, precursory activity in the western half of the array is well resolved (Extended Data Fig. 5). In 2013, North Lake and a small lake (Small Lake, Extended Data Fig. 5) 2 km to the southwest of North Lake may have drained concurrently or in sequence. Positive crack-normal (approximately northward) motion during the North Lake hydro-fracture was

observed at the three GPS stations located between Small Lake and North Lake (NL08, NL07, NL10). This can be seen in the positive crack-normal excursion of 0.1 m at station NL08, 0.25 days after the 2013 maximum North Lake hydro-fracture crack opening (Fig. 2c).

Available imagery does not capture the precise timings of the lakes' drainages. The last WorldView image obtained on 6/17/2013 (2 days before the 2013 North Lake drainage) shows a filled North Lake and Small Lake. The volume of North Lake (Small Lake) was at least $0.0036 \pm 0.001 \text{ km}^3$ ($0.0021 \pm 0.001 \text{ km}^3$) at the time of drainage based on the shoreline positions obtained two days prior to the North Lake drainage event (Extended Data Figs. 2d, 3b). The first post-drainage WorldView image available on 7/5/2013 (16 days after North Lake drainage, Extended Data Fig. 2e) shows an empty North Lake and Small Lake, with a bright, linear crack running through the South Lake basin that could be the 2013 Small Lake hydro-fracture. July 2014 field surveys confirmed the existence and East-West strike of the Small Lake hydro-fracture.

In an attempt to distinguish 2013 North Lake and Small Lake hydro-fracture events, a NIF including an additional source of displacement as a vertical plane with tensile opening along the South Lake hydro-fracture crack trace was developed and run with the 2013 GPS data. The NIF with the additional Small Lake hydro-fracture ("four-source") did not accurately capture opening and closing along the Small Lake hydro-fracture. While including the Small Lake hydro-fracture more completely fits NL07, NL08, and NL10 station motion during the 1.5 hours following the North Lake rapid drainage, the NIF results for the Small Lake hydro-fracture exhibit unrealistic behavior by continuing to widen throughout the day after North Lake drainage. We attribute this

result to the nonuniqueness inherent in the inversion due to the lack of stations between North and Small Lake. Because the NIF results including the Small Lake source produce a physically unlikely result (a crack that continues widening after drainage) we favor the alternate solution which fits the data equally well—namely no Small Lake hydro-fracture and a rougher distribution of basal slip/opening ($\gamma=500$) that accounts for the crack-normal component oscillations at NL07 and NL08 via the spatial propagation of the basal slip patch (Fig. 2c).

For a NIF that does not include the additional Small Lake vertical plane (“three-source”), individual station motion can be mapped onto the three original deformation sources (vertical opening, basal cavity opening, and basal slip) with a highly spatially resolved basal plane ($\gamma=500$) and associated highly temporally resolved vertical plane ($\alpha = 500$). The three-source 2013 NIF yields realistic opening and closing North Lake hydro-fracture behavior. We present the three-source 2013 NIF results here, since we cannot sufficiently distinguish between the North and Small Lake drainages from the available station spatial density.

Independent of the NIF setup (3 or 4 sources of displacement), precursory activity in the western half of the array is well resolved in the GPS data. North Lake drained rapidly over a period of ~5 hours beginning at 15:00 local time on June 19, 2013 (DOY 170) (Figs. 2c, f). From analysis of WorldView imagery, the 2013 west North Lake shoreline had not reached M1 two days before the drainage event (Extended Data Fig. 3b), though, in the absence of a snow-dam, water could have reached the moulin via a deeply incised surface melt-water channel (Extended Data Fig. 2d). During the 16 hours leading up to hydro-fracture initiation, flowline parallel speed up of western stations (Fig. 2c) generates considerable M_0 (Fig. 2f), and is

650 coincident with a basal cavity opening of $\sim 0.002 \text{ km}^3$ beneath the North Lake and Small Lake
651 basins (Fig. 2f; Extended Data Fig. 5a–c). Inversion results suggest that hydro-fracture opening
652 begins in the region of M1; however, opening along the eastern portion of the vertical plane is
653 not well constrained due to a lack of GPS stations to the immediate northeast of North Lake
654 basin (e.g. NL05, NL06, and NLBS). As in previous years, during the North Lake rapid drainage
655 basal cavity opening occurs beneath the lake basin, while extra basal slip extends further afield
656 (Extended Data Fig. 5d–f; Movie 3). A ground survey of North Lake basin a month after the
657 2013 NL drainage identified post-drainage supraglacial melt-water routing through M2
658 (Extended Data Fig. 1).

Methods References:

33. Chen, G. GPS kinematics positioning for the Airborne Laser Altimetry at Long Valley, California. 173 (1998).
34. Bevis, M. *et al.* Bedrock displacements in Greenland manifest ice mass variations, climate cycles and climate change. *Proc. Natl. Acad. Sci. U. S. A.* **109**, 11944–8 (2012).
35. Moratto, Z. M., Broxton, M. J., Beyer, R. A., Lundy, M. & Husmann, K. Ames Stereo Pipeline, NASA's Open Source Automated Stereogrammetry Software. *41st Lunar Planet. Sci. Conf.* (2010).
36. Van Angelen, J. H., van den Broeke, M. R., Wouters, B. & Lenaerts, J. T. M. Contemporary (1960–2012) evolution of the climate and surface mass balance of the Greenland ice sheet. *Surv. Geophys.* **35**, 1155–1174 (2013).
37. Okada, Y. Surface deformation due to shear and tensile faults in a half-space. *Bull. Seismol. Soc. Am.* **75**, 1135–1154 (1985).
38. Miyazaki, S. A transient subduction zone slip episode in southwest Japan observed by the nationwide GPS array. *J. Geophys. Res.* **108**, 2087 (2003).
39. Miyazaki, S., Mcguire, J. J. & Segall, P. Seismic and aseismic fault slip before and during the 2011 off the Pacific coast of Tohoku Earthquake. *Earth, Planets Sp.* **63**, 637–642 (2011).
40. Van der Veen, C. J. Fracture mechanics approach to penetration of surface crevasses on glaciers. *Cold Reg. Sci. Technol.* **27**, 31–47 (1998).
41. Hobbs, P. V. *Ice physics*. (Clarendon Press, 1974).
42. Kanamori, H. Magnitude scale and quantification of earthquakes. *Tectonophysics* **93**, 185–199 (1983).
43. Glen, J. W. The creep of polycrystalline ice. *Proc. R. Soc. A Math. Phys. Eng. Sci.* **228**, 519–538 (1955).
44. Budd, W. F. & Jacka, T. H. A review of ice rheology for ice sheet modeling. *Cold Reg. Sci. Technol.* **16**, 107–144 (1989).
45. Kamb, B. & Echelmeyer, K. a. Stress-gradient coupling in glacier flow: I. Longitudinal averaging of the influence of ice thickness and surface slope. *J. Glaciol.* **32**, 267–284 (1986).

689 46. Hindmarsh, R. C. a. The role of membrane-like stresses in determining the stability and
690 sensitivity of the Antarctic ice sheets: back pressure and grounding line motion. *Philos.*
691 *Trans. A. Math. Phys. Eng. Sci.* **364**, 1733–1767 (2006).

692

Extended Data Figure Captions.

Extended Data Table 1.

2011, 2012, and 2013 North Lake Drainage Environmental, GPS, and Network Inversion Filter observations. Time of start of precursor, start of hydro-fracture crack opening, and maximum hydro-fracture crack opening equivalent to time delineations in Fig. 2.

Extended Data Fig. 1

July 21, 2011 WorldView image of an empty North Lake basin after the 2011 rapid drainage event. Yellow outline shows M1 and M2 location along the hydro-fracture trace (endpoints marked by black arrows). Yellow triangles mark GPS stations within the map area. Image © 2011 DigitalGlobe, Inc.

Extended Data Fig. 2

Images and Digital Elevation Model (DEM) of 2011 and 2013 North Lake basin. Panel a (d) shows the WorldView image chosen to map the 2011 (2013) North Lake pre-drainage shoreline position. Panel b (e) shows the WorldView image of an empty North Lake basin obtained July 21, 2011 (July 5, 2013) used to create the 2011 (2013) North Lake DEM. Panel c (f) shows the 2-meter horizontal resolution DEM (2-m vertical contours in black) for the North Lake region, with the North Lake shoreline (red), M1 (yellow), and hydro-fracture trace (blue) mapped over contours. Images © 2011 and 2013 DigitalGlobe, Inc.

Extended Data Fig. 3.

2011 and 2013 North Lake Depths. 2-m resolution Digital Elevation Models (DEM) were created from the first available post-drainage WorldView stereo pair obtained of the region in (a) 2011 and (b) 2013. Shoreline positions from 2011 and 2013 derived from last pre-drainage WorldView or TerraSAR-X images obtained over the region are shown in red. The last pre-drainage WorldView image for 2011 occurs 2 days prior to the drainage event on June 17, 2011; the last pre-drainage SAR image for 2013 occurs 1 day before the event on June 17, 2013. Filling the empty basin DEM up to the greatest known pre-drainage shoreline extent generates North Lake depths (1-m vertical contours in black) are generated in relation to the greatest known pre-drainage shoreline extents and are used to calculate minimum 2011 and 2013 North Lake pre-drainage volumes. The trace of the vertical hydro-fracture crack is shown in grey; M1 is outlined in yellow.

Extended Data Fig. 4.

2012 Basal slip and cavity opening at hydro-fracture initiation and maximum hydro-fracture opening. NIF-calculated (a) extra basal slip accumulated, (b) basal cavity opening, and (c) hydro-fracture crack opening at the time of the 2012 (a–c) hydro-fracture initiation and (d–f) maximum hydro-fracture opening (time points shown in Fig. 2a). Moulin location, last known lake shoreline, GPS stations, and NIF vertical crack surface trace derived from SAR imagery are shown as a yellow circle, blue line, black triangles, and black line, respectively. Vector fields show GPS (NIF) displacement less background velocities in black (green) for (a) the period between the start of the precursor and hydro-fracture initiation, and (d) the period between hydro-fracture initiation and maximum hydro-fracture opening. Error ellipses of 1 sigma are

shown for the GPS displacements (blue ellipses). Basal subelements are 0.83 km by 0.83 km, resulting in 144 subelements over a 10 km by 10 km region.

Extended Data Fig. 5.

2013 Basal slip and cavity opening at hydro-fracture initiation and maximum hydro-fracture opening. NIF-calculated (a) extra basal slip accumulated, (b) basal cavity opening, and (c) hydro-fracture crack opening at the time of the 2013 (a–c) hydro-fracture initiation and (d–f) maximum hydro-fracture opening (time points shown in Fig. 2a). Moulin location, last known lake shoreline, GPS stations, and NIF vertical crack surface trace derived from SAR imagery are shown as a yellow circle, blue line, black triangles, and black line, respectively. Vector fields show GPS (NIF) displacement less background velocities in black (green) for (a) the period between the start of the precursor and hydro-fracture initiation, and (d) the period between hydro-fracture initiation and maximum hydro-fracture opening. Error ellipses of 1 sigma are shown for the GPS displacements (blue ellipses). Basal subelements are 0.83 km by 0.83 km, resulting in 144 subelements over a 10 km by 10 km region.

Extended Data Fig. 6

2011 Station Timeseries. (a) Flowline, (b) crack-normal, and (c) uplift GPS displacements (meters) (grey stars) for stations used in the 2011 NIF. NIF station fits from the three displacement sources (Extended Data Fig. 7) shown in red, and NIF station fits including $L(t)$ (random benchmark wobble term) are shown in black. Stations are ordered roughly north to south on the y-axis, offset by 0.5 meters.

Extended Data Fig. 7

2011 NL08 and NL04 Station flowline, crack-normal, and uplift displacements computed from NIF displacement sources. Flowline, crack-normal, and uplift GPS displacements less background velocity field (grey stars) are plotted for (a–c) NL04 and (d–f) NL08 over the two days before and one day following the 2011 rapid NL drainage. These stations are two examples chosen from the full array because they capture displacement on both the northern (NL04) and southern (NL08) side of the lake, are located at roughly the same longitude as M1, and are within 2 km of the lake. NIF calculated surface ice displacements at NL04 and NL08 stations from the three displacement sources are plotted for the (red) hydro-fracture crack opening, (green) basal cavity opening, and (blue) extra basal slip. The sum of all three NIF displacement sources is shown in black.

Extended Data Fig. 8

Maximum Likelihood Estimation of NIF Hyperparameters. Maximum likelihood estimation of the vertical hydro-fracture plane temporal smoothing parameter, α , for (a) 2011, (b) 2012, and (c) 2013 NIF. The maximum likelihood estimation corresponds with the minimum value on the $-2 \times \text{Likelihood}$ plots¹⁹. Minimum likelihood estimates are outlined in red circles, with the value used in each year's inversion outlined indicated with a black diamond (Methods).

Extended Data Fig. 9

Stress changes across North Lake basin during (a) supraglacial lake formation, (b) rapid drainage precursor, and (c) hydro-fracture opening.

Supplementary Information:

Supplementary Information Movies 1-3 Captions

Movie 1

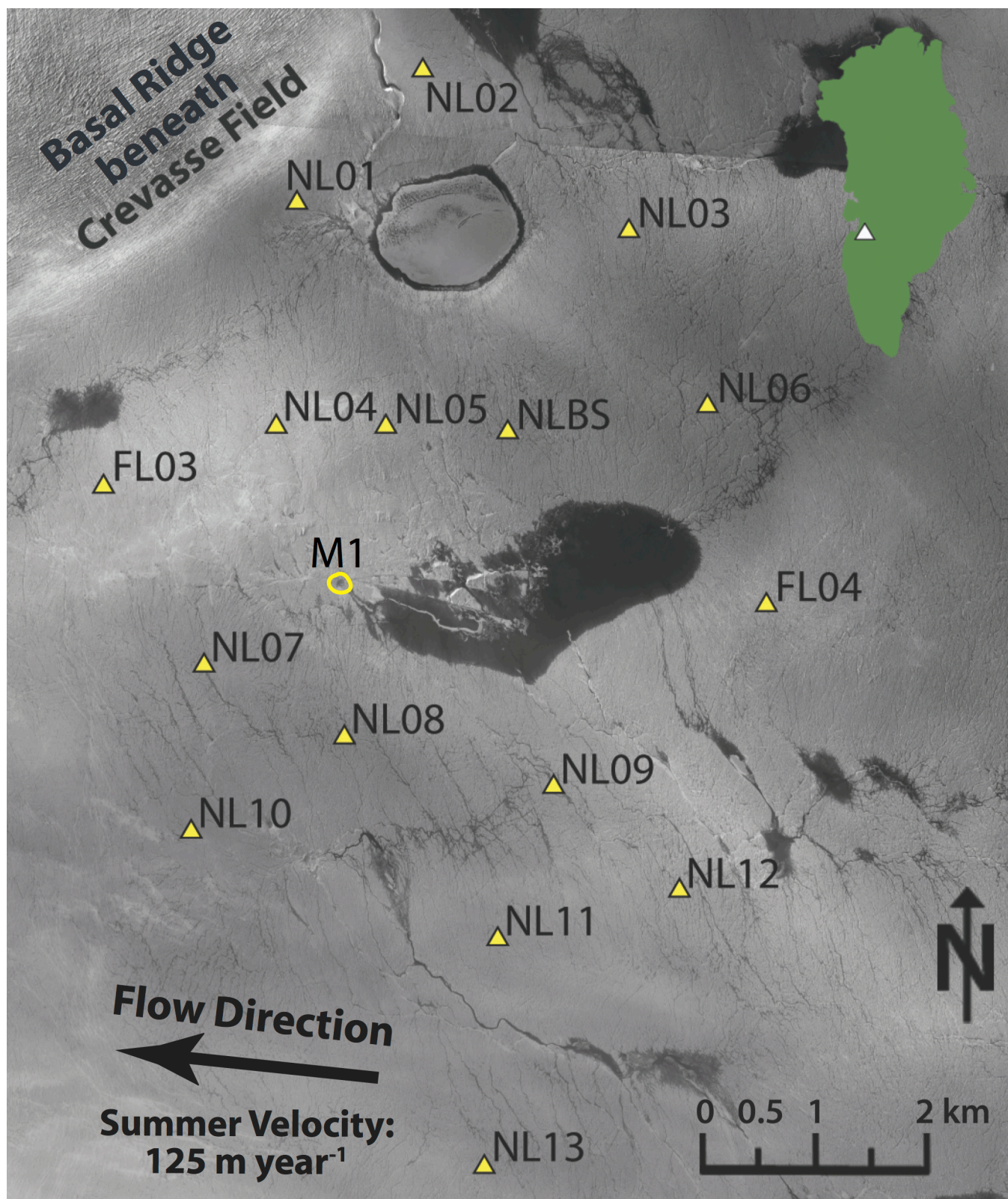
Hydro-fracture crack opening, basal cavity opening, and additional basal slip during the 2011 North Lake rapid drainage. Movie spanning the two days prior and one day following the 2011 drainage event, depicting (d) opening along the hydro-fracture crack as a percentage of the maximum opening (Extended Data Table 1) of the hydro-fracture crack, (e) basal cavity opening, and (f) additional basal slip above background velocity values for all NIF subelements. GPS stations are shown with black triangles; station NL08 is shown as a white triangle. The yellow box outlines the subelement of maximum opening, uplift, or slip within the hydro-fracture crack, basal cavity opening, and basal slip planes, respectively, once opening or slip has exceeded a threshold value of 20% of maximum opening for the hydro-fracture crack and 0.2 m basal cavity opening or additional basal slip for the basal planes. Station fit between GPS station NL08 and the NIF is shown in the left column, with NL08 (a) crack-normal, (b) uplift, and (c) along flowline displacements less background velocities in grey, and the NIF inversion at the location of NL08 in black. The blue diamond follows the NIF inversion at the location of NL08 along the time of the NIF panels. “Start of Precursor,” “Hydro-fracture Initiation,” and “Maximum Hydro-fracture Opening” times are marked as vertical grey lines are at the same time points delineated in Fig. 2 and Extended Data Table 1.

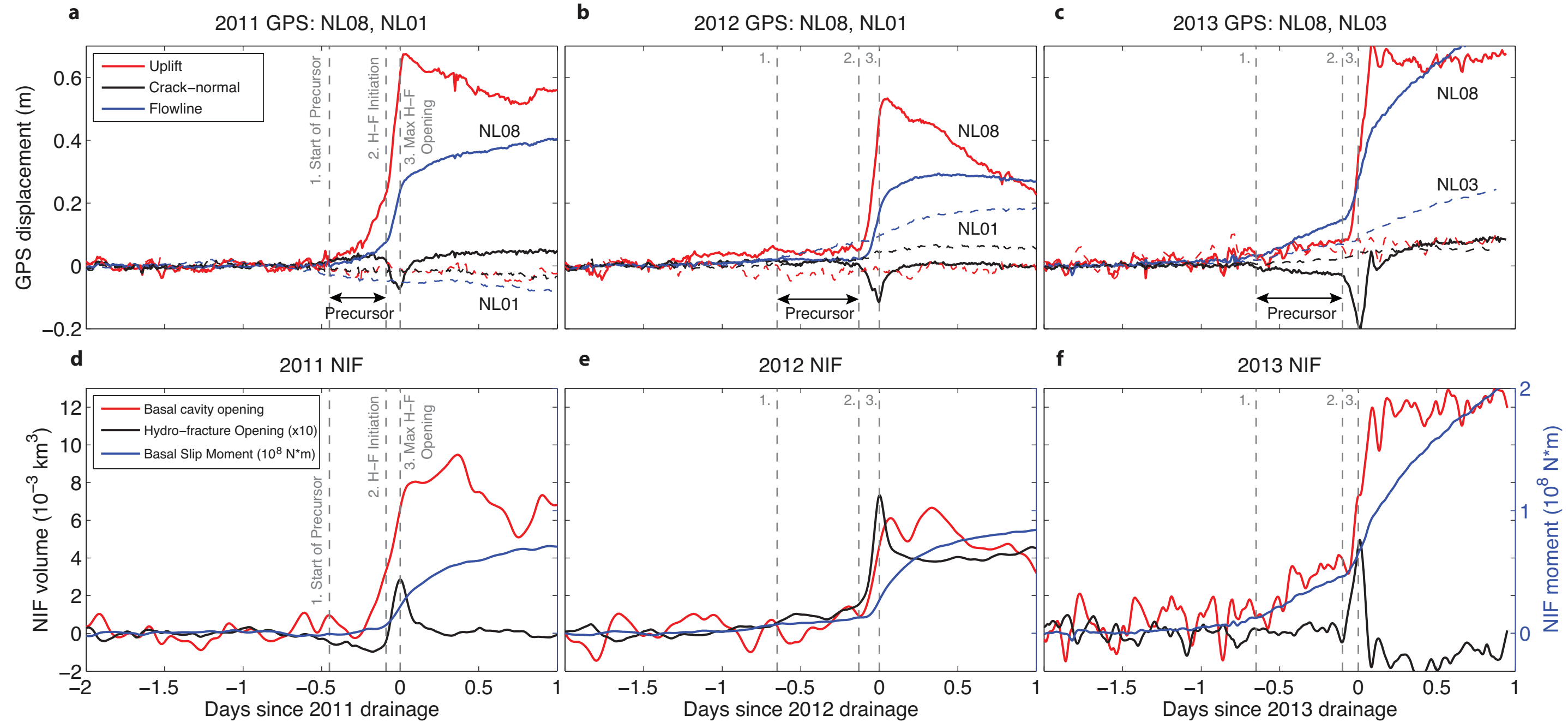
Movie 2

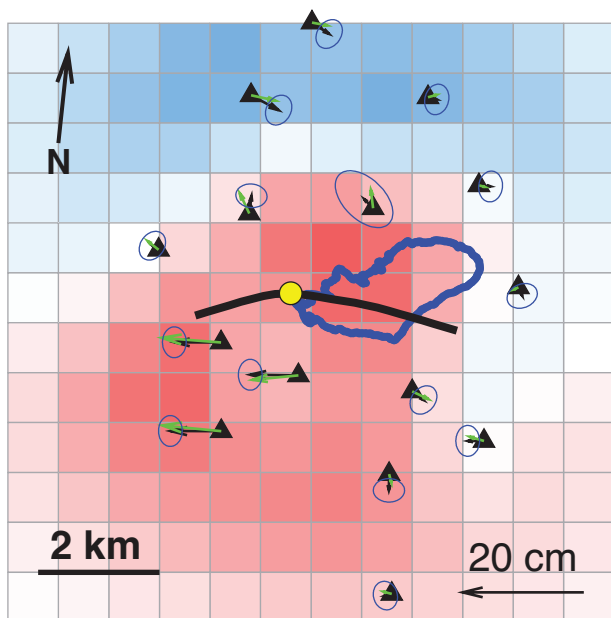
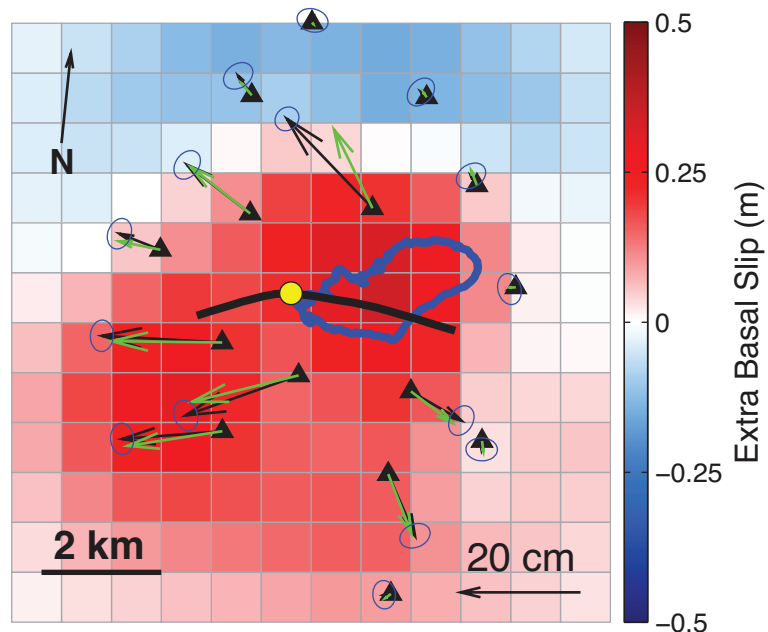
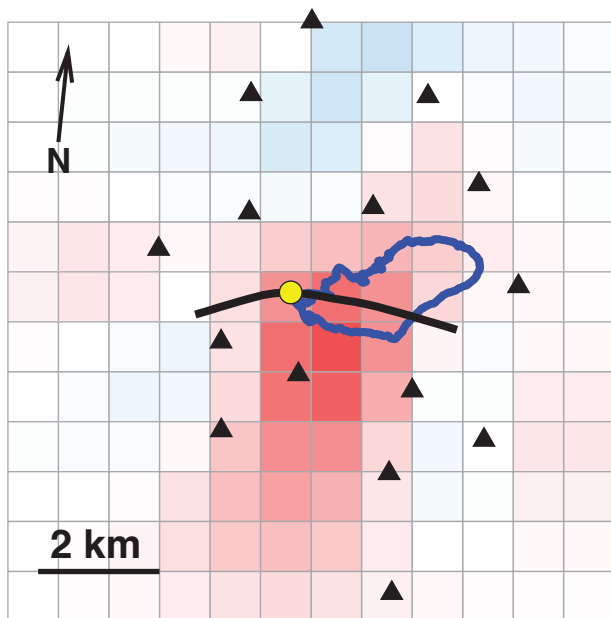
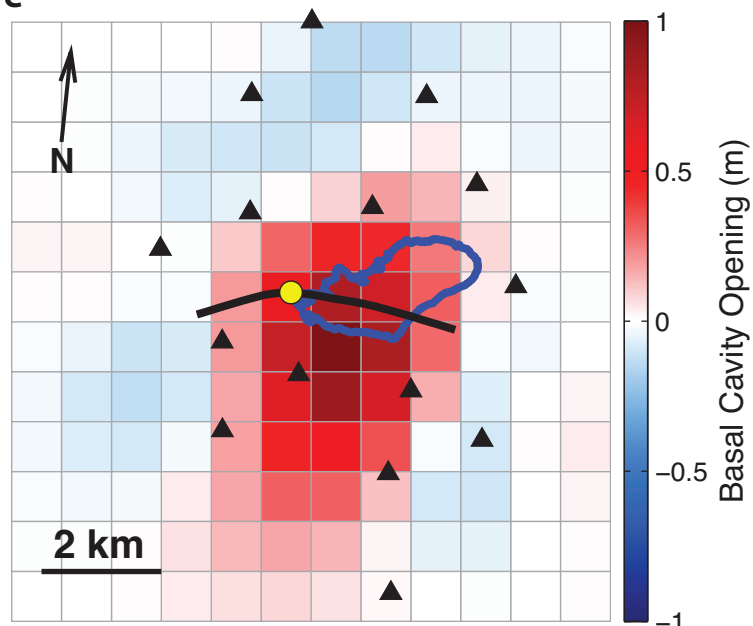
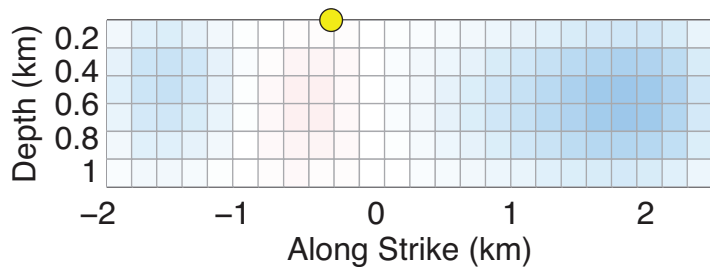
Hydro-fracture crack opening, basal cavity opening, and additional basal slip during the 2012 North Lake rapid drainage. Same as Movie 1 but for the 2012 North Lake rapid drainage.

Movie 3

Hydro-fracture crack opening, basal cavity opening, and additional basal slip during the 2013 North Lake rapid drainage. Same as Movie 1 but for the 2013 North Lake rapid drainage.





a 2011 Hydro-fracture Initiation DOY 169.21**d** 2011 Max Hydro-fracture Opening DOY 169.32**b****e****c****f**